




Facet-dependent magnetic properties of magnetite nanoparticles coated with dodecyl amine and their biological effect in hepatocarcinoma cell line

Yareli Rojas-Aguirre^{1,*}, Juan Rizo², Miguelina Martínez-Aguilera¹, Adriana Rodríguez-Hernández³, Beatriz Díaz-Bello³, Genaro Vázquez-Victorio³, Héctor Domínguez¹, Rubén Mendoza-Cruz¹, Israel Betancourt¹, Saret Ortega-Galindo¹, and Patricia Guadarrama^{1,*} 

¹ Instituto de Investigaciones en Materiales, Universidad Nacional Autónoma de México, Circuito Exterior S/N, Ciudad Universitaria, Coyoacán 04510, México

² Departamento de Ciencias, Instituto Tecnológico y de Estudios Superiores de Monterrey (ITESM), Campus Ciudad de México, Tlalpan 14380, México

³ Departamento de Física, Facultad de Ciencias, Universidad Nacional Autónoma de México, Circuito Exterior S/N, Ciudad Universitaria, Coyoacán 04510, México

Received: 25 July 2023

Accepted: 2 December 2023

Published online:

4 January 2024

© The Author(s), 2024

ABSTRACT

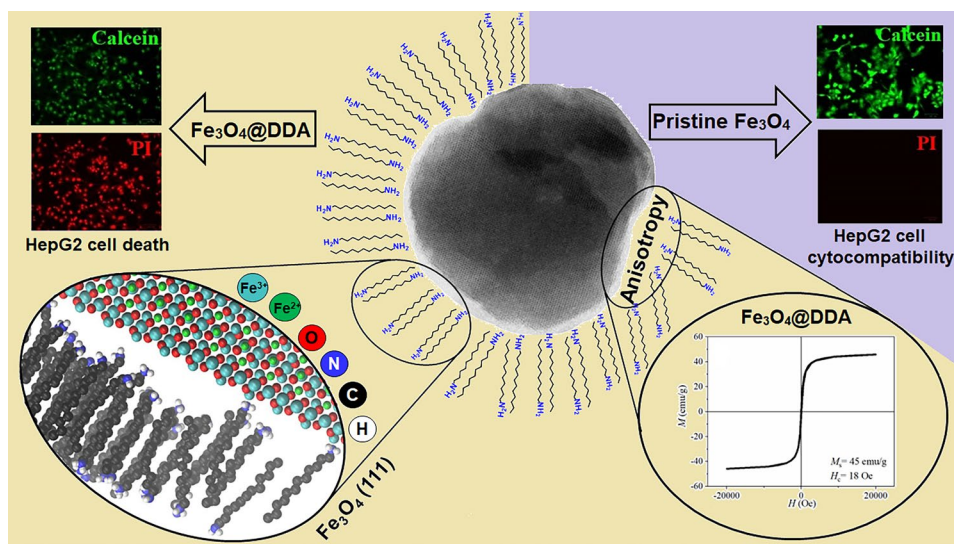
Herein was conducted a compelling structural analysis of magnetite nanoparticles (NPs) coated with dodecyl amine (DDA), compared with uncoated magnetite, both previously synthesized by an accelerated one-pot synthesis, starting from a single iron precursor. XRD/TEM results for the obtained nanomaterial $\text{Fe}_3\text{O}_4@$ DDA showed the predominance of Fe^{3+} cations on the most stable atomic plane of magnetite (111). Using Molecular Dynamics calculations, with the observed atomic dispositions as inputs, it was established that NPs' surface and DDA might interact by short-distance coordination, with DDA as a ligand of Fe^{3+} cations, or by long-distance adsorption via H-bonding. The simulations align with TEM images, revealing an amorphous contour corresponding to the organic coating arranged as a bilayer. The TGA analysis corroborated a dual mass loss profile relating to the DDA bilayer at 116 °C and 350 °C. The $\text{Fe}_3\text{O}_4@$ DDA NPs' magnetic properties (saturation magnetization (M_s) and coercivity field (H_c)) were preserved. $\text{Fe}_3\text{O}_4@$ DDA exhibited a reduction of 3 emu/g in M_s and an increment of 12 Oe in H_c , compared with Fe_3O_4 NPs, attributable to the coating inhomogeneity and the consequent anisotropy rise. $\text{Fe}_3\text{O}_4@$ DDA triggered concentration-dependent cytotoxic effects on the human hepatocarcinoma cell line HepG2. At 50 $\mu\text{g}/\text{mL}$ after incubation of 48 h, cell viability was 63% <, whereas at 72 h only 30% of cells were viable. At 300 $\mu\text{g}/\text{mL}$, less than 10% of HepG2 cells remained viable after 24 h of incubation. In the case of Fe_3O_4 NPs assessed in the same cell line, cell viability remained as high as 80% at 300 $\mu\text{g}/\text{mL}$ during 72 h of incubation.

Handling Editor: Dale Huber.

Address correspondence to E-mail: yareli.rojas@materiales.unam.mx; patriciagua@materiales.unam.mx

Trypan blue assay suggests membrane integrity damage as the primary mechanism of HepG2 cell death. Even though the *in vitro* results herein presented are preliminary, they represent the first report of the cytotoxic effect of magnetite coated with a nitrogenous surfactant.

GRAPHICAL ABSTRACT



Introduction

The significant advances in synthetic approaches have brought new horizons in the design and engineering of tailored materials at the nanometer scale through precise control over size, shape, composition, and surface properties [1]. Particularly, magnetic nanoparticles (NPs) have positioned at the forefront of scientific and technological research in different areas such as environmental remediation for water treatment and pollutants removal [2, 3], energy and data storage [4], catalysis [5], magnetic sensing [6, 7] and biomedical applications [8]. Among magnetic materials, magnetite (Fe_3O_4) NPs have gathered continuous scientific interest due to their accessibility and modifiability. Furthermore, its suitable behavior of biocompatibility converts the magnetite also to a biologically attractive material [9]. The surface modification of magnetite with different coatings such as polymers, surfactants, or biomolecules, alone or in combination, under the conception of surface engineering [10], has played a crucial role in protecting the magnetic core from oxidation and improving its colloidal stability as it may reduce in different extents the aggregation by electrostatic or steric repulsion, but more importantly,

has allowed inducing controlled responses, either biological or magnetic, among others. In the field of nanomedicine, diverse iron oxide organic coated NPs have been designed as stimuli-response materials for controlled drug release [11, 12]. Other therapeutic approaches like magnetic resonance imaging and hyperthermia have also shown progress due to the possibility of obtaining multifunctional NPs by the coating of magnetite [13].

Regarding the magnetic response, recent reports have shown that depending on the functional groups and thickness, the organic coatings may offer a versatile and effective means of tuning the saturation magnetization, the magnetic anisotropy, and coercivity of magnetic NPs [14] by their ability to reduce the surface spin disorder, completing some external coordination sphere sites of the metallic ions [15].

Given the importance of magnetite in different fields, and the relevance of incorporating organic coatings in the context of surface engineering, we reported previously a facile one-pot synthesis of Fe_3O_4 NPs, either uncoated and coated with the surfactant dodecyl amine (DDA), starting from FeCl_2 as a single iron precursor, and under a non-conventional longitudinal stirring regime [16]. The characterization results

evidenced the obtaining of magnetite-coated NPs with nearly spherical shape. The magnetic measurements showed that the coated NPs ($\text{Fe}_3\text{O}_4@\text{DDA}$) exhibited a higher saturation magnetization (M_s) and smaller coercivity (H_c) than the uncoated ones, presumably as an effect of the reduction in the surface disorder, and the concomitant decrease in the particle anisotropy, as observed in other reports [17]. Nevertheless, contrary results where a decrease in the saturation magnetization is observed after surface modification have also been informed [18]. Therefore, it is of interest to investigate the correlation between the surface structure obtained in the synthesis, not only with the magnetic behavior related to stimulus–response features but also with the biological profile of these nanoobjects, which is a very active field of research [19]. In this regard, uncoated iron oxide NPs have been extensively investigated. Current studies have allowed the identification of different cellular signaling pathways affected by their presence [20], and also the possible cellular death triggered by them has been determined [21], along with the identification of lysosomes as the organelles responsible for regulating the nanoparticles' cellular responses [22]. However, when coatings are present, cytotoxic cell response may depend on various factors such as surface chemistry, size, preparation method, and dose [23, 24]. Consequently, it is crucial to perform *in vitro* assays to establish a correlation between the nature of the coatings and their potential toxicity when considering the application of coated iron oxide NPs in different therapies.

The present study focuses on the comprehensive structural characterization of uncoated magnetite NPs by conducting a detailed analysis of X-ray diffraction (XRD) and transmission electron microscopy (TEM) results. We aim to provide relevant information about the exposed atoms on the magnetite's most stable and commonly observed atomic plane (111) to be used as a tailored magnetic NPs design strategy.

By delving deeper into the structural properties of uncoated magnetite nanoparticles, we provide significant information that can aid in the development of tailored nanomaterials with enhanced functionalities, in this case, DDA as a coating to obtain $\text{Fe}_3\text{O}_4@\text{DDA}$ NPs.

Therefore, the identified atomic positions of oxygen and $\text{Fe}^{3+}/\text{Fe}^{2+}$ cations in the unit cell of the NPs were used as a solid foundation for constructing a robust theoretical model which provided an overall understanding of the intricate interactions between the

NPs and the surfactant DDA, unraveling key insights into the distribution of DDA on the surface of the NP and the orientation of its polar heads. By employing advanced molecular dynamics simulations and incorporating water molecules into the system, we went beyond the scope of earlier studies, inquiring into the dynamic behavior between DDA and the NP [25, 26]. Theoretical findings, supported by structural analysis, unveiled the interactions between DDA coating and the surface of the NP that, in turn, were correlated with the magnetic properties of the magnetite NPs.

In addition, we aimed to explore the biological behavior of $\text{Fe}_3\text{O}_4@\text{DDA}$ NPs through the evaluation of their cytotoxic profile on HepG2 cells as an *in vitro* model for hepatocellular carcinoma (HCC). HCC is recognized as the sixth most prevalent malignancy and the fourth leading cause of cancer-related deaths globally [27]. Cell viability assays were evaluated by the calcein AM/propidium iodide double staining assay to differentiate between live and dead cells. We also evaluated the cell viability of Fe_3O_4 NPs as a reference. In order to approach the cell death mechanism, we performed the Trypan blue dye exclusion assay. As far as we know, this is the first examination of $\text{Fe}_3\text{O}_4@\text{DDA}$ NPs cytotoxicity in HepG2 cells and it is also the first time that the cell viability of Fe_3O_4 NPs is determined through the calcein AM/propidium iodide double staining assay.

Materials and methods

Synthesis

As described in our previous report [16], Fe_3O_4 NPs uncoated and coated with dodecyl amine (DDA) may be obtained by one-pot synthesis, starting from a single iron precursor ($\text{FeCl}_2\cdot 4\text{H}_2\text{O}$) in alkaline aqueous solution, and open atmosphere conditions. Briefly, the synthesis is based on adding KOH to an aqueous solution of $\text{FeCl}_2\cdot 4\text{H}_2\text{O}$ on a rotary evaporator for 5 min at 90 °C to obtain Fe_3O_4 NPs until reaching a final pH value of 11. To obtain $\text{Fe}_3\text{O}_4@\text{DDA}$, an emulsion of DDA and KOH in ultrapure water was formed and mixed with an aqueous solution of $\text{FeCl}_2\cdot 4\text{H}_2\text{O}$, under the same conditions mentioned above. Fe_3O_4 or $\text{Fe}_3\text{O}_4@\text{DDA}$ NPs were obtained as a black precipitate, decanted with a neodymium magnet, washed several times with water/acetone, and then freeze-dried.

Structural characterization of Fe₃O₄ and Fe₃O₄@DDA NPs

X-ray Powder diffraction

The crystal structure and the spinel phase of Fe₃O₄ and Fe₃O₄@DDA were determined through XRD in a Bruker D8 Advance X-ray diffractometer using Cu-K α radiation ($\lambda = 1.541874 \text{ \AA}$) operating at 30 kV and 30 mA with a scanning speed of $0.5^\circ 2\theta/\text{min}$ in the range of 20° – 80° .

Transmission electron microscopy (TEM)

Scanning transmission electron microscopy (TEM-STEM) was performed in a JEOL ARM-200F microscope at the LUME@IIM and operated at 200 keV. For image acquisition, the high-angle annular dark-field (HAADF) detector was set with a collection semi-angle of 68 – 280 mrad , while the bright-field (BF) detector was set to $\sim 18 \text{ mrad}$. The convergence semi-angle was set to 24 mrad . Samples were mounted on standard 300-mesh carbon-coated Cu grids, placing a small drop of the colloidal solution on them and letting them dry completely before characterization.

Thermogravimetric analysis TGA

Thermogravimetric analysis was performed to investigate the relative content of DDA in the magnetite NPs. To that aim, experiments were carried out in a TA instrument Q600 V8. For their analysis, approximately 10 mg of each sample was placed in a platinum tray and heated at 10° C/min under N₂ atmosphere.

Magnetic properties

Room temperature magnetic properties of Fe₃O₄@DDA and Fe₃O₄ were measured by vibrating sample magnetometer by a Quantum Design Magnetic Physical Measurement System (MPMS3) at maximum applied field of 2 T. Saturation magnetization and coercivity field were determined from hysteresis loops of each NPs sample.

Computational simulations

Molecular dynamics was conducted for a magnetite crystal (Fe₃O₄) using a unit cell with parameters $a = b = c = 8.4$ in a rhombic box of dimension $4.736 \times 4.10152 \times 7.0 \text{ nm}$. Simulations were carried out for the (111) face with tetrahedral Fe exposed on the surface as shown in reference [25].

All atoms in the magnetite were treated as Lennard Jones (LJ) sites for the potential interaction, with parameters obtained from reference [26] and using partial charges 2^+ and 3^+ for iron atoms (Fe), and 2^- for oxygen (O). These set of LJ parameters reported in the literature showed good agreement with experimental data for adsorption and structure of water at magnetite surfaces [26]. For the DDA molecules, a united atom model was simulated, where all CH_n groups in the tail were joint in one single site, whereas the headgroup was explicitly modeled. The Force field for the DDA was taken from the literature [28], while the water molecules were modeled by the SPC/E model [29]. Initial configurations were constructed with DDA molecules close to the magnetite NPs with the headgroups facing the surface. On the top of the DDA, 2197 water molecules were placed and simulations were conducted for different number of DDA molecules.

All simulations were performed with GROMACS-21 software [30], using periodic boundary conditions in all directions. Simulations were carried out in the NVT ensemble at constant temperature using the V-scale thermostat with a relaxation time constant of 0.1 ps. The electrostatic interactions were handled with the particle mesh Ewald method, and the short-range interactions were cutoff at 10 \AA . Bond lengths were constrained using the Lincs algorithm. The simulations were performed for 80 ns after 10 ns of equilibration with a timestep of $dt = 0.002 \text{ ps}$.

Biological assays

Cell culture

Human hepatocarcinoma cells HepG2 (HB-8065, ATCC) were grown in Eagle's Minimum Essential Medium (MEM) supplemented with 10% Fetal Bovine Serum (FSB), 1 mM sodium pyruvate and 10 U/mL penicillin and 10 $\mu\text{g/mL}$ streptomycin (Gibco, Thermo Fisher Scientific). Cells were maintained at 37° C in a 5% CO₂ atmosphere in a humidified incubator and passed up

to 1:4 dilution with 0.25% trypsin before experimental seeding.

Cell viability assay

To determine the susceptibility of HepG2 cells to Fe₃O₄@DDA, 1.5 × 10⁴ cells were seeded on collagen-deposited 20 mm round coverslips in a 12-well plate under growth conditions. After 24 h, the medium was removed, and fresh medium containing 10, 50, or 300 µg/mL Fe₃O₄@DDA, sonicated by 5 min, was added to the cells and incubated for 24, 48, or 72 h at growth conditions. After, live/dead cells were assessed through calcein AM/propidium iodide double staining. To that end, 1 µM of calcein AM and 5 µM of propidium iodide (PI) in the serum-free fresh medium were added to the cells and incubated for at least 15 min in the CO₂ incubator. Thereafter, cells were washed once with fresh serum-free MEM to avoid significant fluorescent background. For image acquisition, an epifluorescence microscope Nikon Eclipse Ci-L obtained calcein AM and PI emissions using a 10X/0.3 Plan Fluor DIC objective. Live, dead, and the total number of cells were counted (5 micrographs for calcein AM and IP signals) using FIJI software. Finally, the percentage of viability was computed through Eq. 1 [31]. To assess the effect of the DDA coating on the viability of HepG2 cells, we also evaluated the effect of Fe₃O₄ np under the same experimental conditions. We used deionized water as a vehicle (control).

$$\text{Cell viability\%} = \frac{\text{\#calcein cells(viable)}}{\text{\#IP cells(non viable)} + \text{\#calcein cells(viable)}} * 100\% \quad (1)$$

Statistical analysis

Cell viability experiments were performed independently in a threefold manner. The results were expressed as mean ± standard deviation of three independent experiments. Data were evaluated by analysis of variance (ANOVA), followed by Tukey's Multiple Comparison Test, using GraphPad Prism version 6.0c software. The results were considered statistically significant when $p < 0.05$.

Terminal deoxynucleotidyl transferase (TdT) dUTP Nick-End Labeling (TUNEL) assay

For TUNEL detection, HepG2 cells were fixed with 4% PFA and post-fixed in a pre-chilled 2:1 ethanol:acetic acid solution for 5 min at -20 °C. After fixation, samples were processed according to the manufacturer's instructions described in the ApopTag fluorescein in situ apoptosis detection kit manual (Millipore). TUNEL signal was contrasted with DAPI (1:1000) in DPBS 1X and samples were mounted with Mowiol for preservation before imaging. Each sample was captured in an epifluorescence microscope (Thunder, Leica, Wetzlar, Germany) using a 10X or 40X objective lens. All the images were analyzed with Fiji free software.

Cell membrane integrity

Trypan blue dye exclusion assay was performed to evaluate plasmatic membrane integrity in response to the iron oxide nanomaterials. To that end, 5 × 10⁴ HepG2 cells/well were incubated in growth medium at 37 °C and 5% CO₂. After 24 h of culture, cells were treated with Fe₃O₄@DDA or Fe₃O₄ diluted in MEM medium at the concentration of 300 µg/mL. We also investigated the effect of pristine DDA, evaluated at 72 µg/mL, as an estimate of DDA concentration found in 300 µg/mL of Fe₃O₄@DDA. After 1, 3, or 5 h of incubation, cells were washed once with 1 mL of DPBS 1X and immersed in 0.2% trypan blue solution to visualize cells immediately

to identify those cells with altered membrane integrity. Stained cells were observed in bright-field using an inverted microscope Nikon Eclipse Ti-S and a 10X/0.3 Plan Fluor DLL objective. Permeabilized cells, used as control of non-membrane integrity, were achieved with 1% Triton X-100 in a CO₂ incubator for 10 min and stained as treated cells. Cell membrane integrity was also confirmed by calcein AM and PI double staining as described above.

Results and discussion

XRD

Magnetite NPs, as well as dodecyl amine (DDA) coated magnetite NPs ($\text{Fe}_3\text{O}_4\text{@DDA}$) were synthesized using the experimental procedure previously reported in the literature [16]. The powder X-ray diffraction (XRD) analyses were carried out to confirm the presence of Fe_3O_4 and $\text{Fe}_3\text{O}_4\text{@DDA}$ NPs. Figure 1 shows

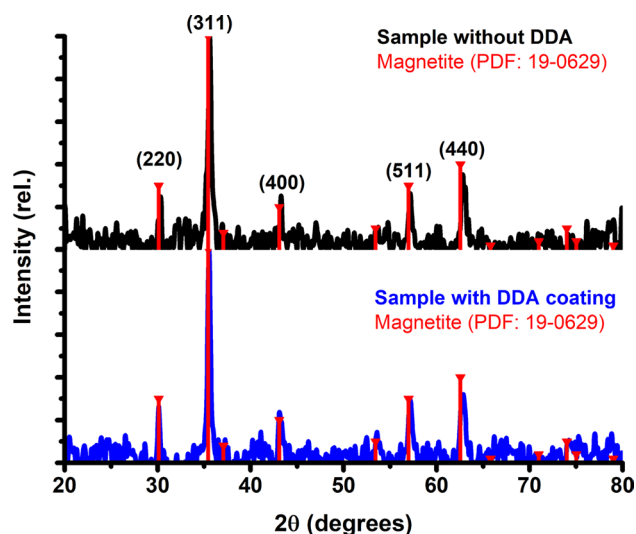


Figure 1 Powder XRD patterns for magnetite NPs without DDA coating (black) as well as coated with DDA (blue); numbers in parenthesis indicate Miller indices.

the XRD results obtained before (black) and after (blue) the DDA coating. As can be seen, the diffraction pattern with five broad peaks at 30.3° , 35.6° , 43.3° , 57.2° and 62.8° correspond to (220), (311), (400), (511) and (440) Miller indices of Fe_3O_4 powder diffraction file (PDF: 19–0629) as already reported in the literature [32, 33]. Also, in Fig. 1 there is no observable change in the XRD patterns before and after the DDA coating suggesting that the magnetite NPs did not oxidize or reduce during the coating process. Another interesting observation of Fig. 1 is the relative intensities of the five peaks, they match the relative intensities of the simulated reference file PDF:19–0629 which suggest that the Fe_3O_4 NPs have spherical morphology [34]. This spherical morphology was also corroborated with TEM images, Figs. 2a, f and 3. Likewise, the calculated crystal domain size (23.1 ± 8.1 nm) using the Scherer's equation is slightly different than the size histogram of TEM (18.5 ± 8.7 nm), implying that there are at least two different crystalline sizes of the NPs. This result is also reflected on the standard deviation values of ± 8.1 nm and ± 8.7 nm which represent 35% and 47% of the average NPs size. Lastly, TEM analyses were also used to identify the presence of magnetite in the samples as well as to identify the facets of the NPs.

TEM

STEM imaging was performed on the synthesized samples to visualize their size and morphology and

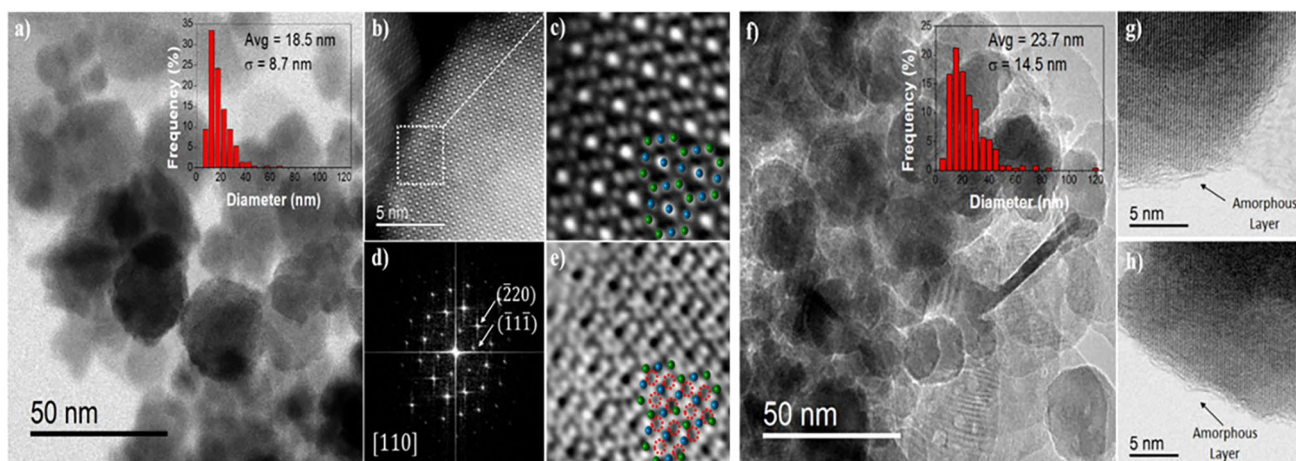


Figure 2 TEM images of **a** low-magnification BF-STEM image of the produced Fe_3O_4 NPs, **b** high-magnification HAADF-STEM image of a single particle, **c** FFT of the selected white squared shown in **b**, **d** zoomed area of the particle in HAADF

mode, **e** zoomed area of the particle in BF mode, **f** low-magnification image of the DDA-functionalized Fe_3O_4 NPs, **g** and **h** zoomed area of the DDA-functionalized Fe_3O_4 NPs in BF mode.

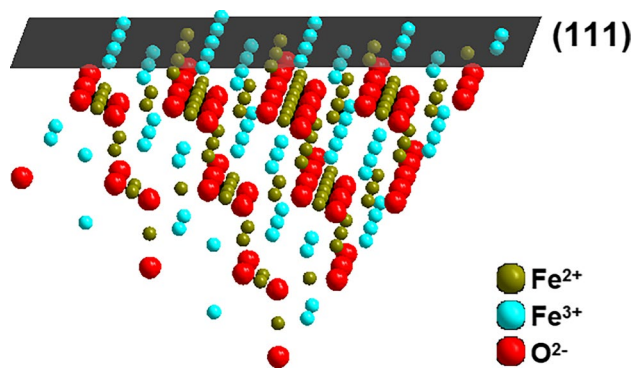


Figure 3 Reconstruction of magnetite cubic inverse spinel structure of the (111) plane using Diamond Crystal and Molecular Structure Visualization software.

corroborate their crystal structure. Figure 2 corresponds to a low-magnification BF-STEM image of the produced Fe_3O_4 NPs. The image shows that the particles were faceted, with an average size of 18.5 ± 8.7 nm. The size histogram is presented as an inset. A high-magnification HAADF-STEM image of a single particle is presented in Fig. 2b the crystal structure was determined through fast-Fourier transform (FFT) analysis. Lattice parameters were obtained by direct measurements of spatial frequencies, Fig. 2c, which reflected the crystal symmetry of the particle. The projected pattern matched the expected Fe_3O_4 -magnetite structure oriented along the [110] zone axis. A zoomed area of the particle, in both HAADF (Fig. 2d) and BF (Fig. 2e) mode, is also shown. The atomic-resolution image enables the direct visualization of atomic column positions and, therefore, the determination of the crystal structure. Figure 2d shows the regular arrangement of the projected positions of iron cations, in which ten columns with lower relative intensity surround high-intensity columns. For comparison, an atomistic model of the regular inverse spinel of magnetite was superposed on both HAADF and BF images. Along the [110] zone axis parallel to the electron beam, atomic columns are composed exclusively of iron or oxygen atoms. Hence, the tetrahedral (green) and octahedral (blue) sites for iron cations are easily determined in HAADF, while oxygen positions (red open circles) can be imaged in BF mode (Fig. 2e).

After functionalization, the DDA-coated Fe_3O_4 NPs were reanalyzed through TEM. A low-magnification image of the DDA-functionalized Fe_3O_4 nanoparticles is shown in Fig. 2f. No notorious change in particle shape was observed after the functionalization

process, while the average size was estimated to be 23.7 ± 14.5 nm. High-magnification BF-STEM images were acquired, focusing on the surface of the particles, attempting to visualize the DDA covering, taking advantage of the enhanced contrast of light elements in BF imaging compared to conventional TEM, Fig. 2g, h. Coverage can be visualized when enough molecules attach to the particle surface, viewed as a carbon-based layer surrounding the particle's surface. A small amorphous layer is observed surrounding the particle's surface, which could be associated with the presence of the organic coating; this conclusion is also supported with thermogravimetric analysis (TGA).

Furthermore, it is known that the (111) plane of Fe_3O_4 is the most thermodynamically stable plane [35, 36]. Hence it is the most observed plane in TEM images (see supplementary material Fig. S1 and S2). Considering this last statement, a reconstruction of magnetite cubic inverse spinel structure was performed to show the surface atoms of magnetite exposed on the [111] facets. Figure 3 shows that Fe^{3+} cations in the tetrahedral sites of the unit cell are predominantly exposed on the surface of magnetite [111] facets, as has been reported elsewhere in the literature [32, 37].

The relevance of categorizing the atomic positions of $\text{Fe}^{3+}/\text{Fe}^{2+}$ cations lies in the opportunity to rationally propose potential interactions with different coatings, such as DDA. The position and predominance of Fe^{3+} cations on the surface of magnetite NPs, along with the atomic positions of oxygen in the unit cell of the NPs, were used in this study to construct a theoretical model able to provide details about the interface interactions between magnetite NPs and the DDA surfactant. As will be discussed, Molecular Dynamics simulations suggest that DDA forms a bilayer structure where the amine groups shape both the inner and outer surface in this ordering. This theoretical result strengthens the description of the TEM images associated to the organic coating of DDA (Fig. 2g, h). Moreover, the ordering that is postulated for the organic coating provides solid arguments to explain the observed cytotoxic activity of the NPs against HepG2 cells, as will be presented below.

TGA

The thermal decomposition of Fe_3O_4 and $\text{Fe}_3\text{O}_4@$ DDA NPs was carried out by heating the samples to 600°C at a rate of $10^\circ\text{C}/\text{min}$ under N_2 atmosphere to obtain the thermogram (TG) profiles that are shown

in Fig. 4. In the case of Fe_3O_4 , a mass loss of less than 2% was observed with a maximum at 37 °C which is associated with the loss of moisture. Furthermore, two mass losses of 5.2% occurring at a maximum of 134 °C and 2.7% occurring at a maximum of 295 °C were observed. Both mass losses correspond to water molecules, either partially coordinated with some surface iron cations (mostly Fe^{3+} as shown in Fig. 3), with maximum mass loss at 295 °C or interacting around the NP through hydrogen bonds (maximum mass loss at 134 °C) as was previously observed [16, 38, 39]. In the case of $\text{Fe}_3\text{O}_4@DDA$, a two-step process was distinguished. The first process at a maximum of 116 °C corresponds to a mass loss of 8.8%, and the second process at a maximum of 350 °C corresponds to 9.7% of the total mass. Anew, the mass loss observed at 116 °C is due to water molecules hydrogen-bonded to the surface of the NPs. Regarding the maximum mass loss at 350 °C, this is due to the organic capping

of DDA around the NPs. Comparing the temperatures of hydrogen-bonded water molecules on Fe_3O_4 (134 °C) and $\text{Fe}_3\text{O}_4@DDA$ (116 °C), it is evident that water molecules are weakly hydrogen-bonded to $\text{Fe}_3\text{O}_4@DDA$ with regards to Fe_3O_4 , but presumably promoting a bilayer arrangement. One very important observation is the mass loss of 2.6% in the $\text{Fe}_3\text{O}_4@DDA$ sample since the DTG curve does not show any maximum mass loss, this is because the mass loss is constant and therefore the derivative does not show any evident change. Nevertheless, this mass loss is most likely due to coordinated water molecules with Fe^{3+} on the surface of the NPs, similar for Fe_3O_4 . Lastly, there is also moisture on the $\text{Fe}_3\text{O}_4@DDA$ sample of less than 1% mass loss at a maximum of 41 °C.

The registered dual profile not only evidenced the presence of DDA coating but also may suggest different types of interactions, in terms of strength, between its primary amine functional groups, and the NPs surface. This outcome is in line with the microscopic analysis discussed above.

Magnetic properties and DDA effect

The investigation of the magnetic properties of coated NPs may yield significant insights into the interplay between the NPs' surface and the coating molecules in terms of their chemical nature. The interaction between the surface cations ($\text{Fe}^{2+}/\text{Fe}^{3+}$ in the case of magnetite) and the organic coating will impact the shape of the NPs, which may render changes in the magnetic properties by modifying the surface spin structure.

In this study, hysteresis loop of magnetization M , as a function of applied field H , are shown in Fig. 5 for Fe_3O_4 and $\text{Fe}_3\text{O}_4@DDA$ NPs, for which a slight variation of the saturation magnetization (M_s) was observed: $M_s = 48$ emu/g and $M_s = 45$ emu/g, respectively, whereas for the coercivity field (H_c) a noticeable increase was recorded for the $\text{Fe}_3\text{O}_4@DDA$ NPs ($H_c = 18$ Oe) relative to the Fe_3O_4 sample ($H_c = 6$ Oe).

According to our analysis of XRD and TEM results, the spherical morphology of the NPs was evidenced, with a predominance of cations Fe^{3+} cations on the surface. Even though there were no significant changes in the NPs morphology after coating with DDA, an amorphous layer was observed around the NP surface by high-magnification images, attributable to the presence of the organic coating. Furthermore, the thermal analysis

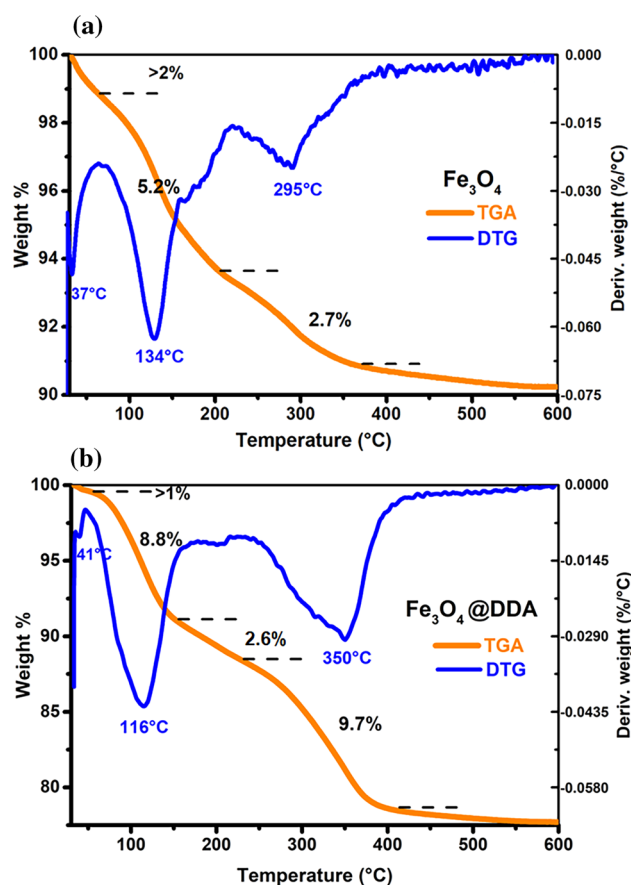
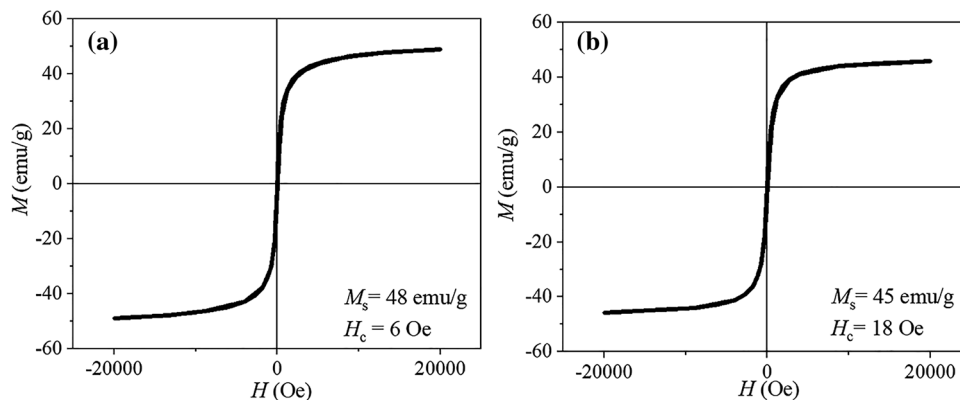


Figure 4 Thermogravimetric analyses (TGA) and derivative thermogravimetry (DTG) of the samples **a** Fe_3O_4 and **b** $\text{Fe}_3\text{O}_4@DDA$ under N_2 atmosphere.

Figure 5 Hysteresis loops M-H for: a) Fe_3O_4 and b) Fe_3O_4 @DDA.



outcomes obtained by TGA not only confirmed the presence of DDA but also suggested a bilayer-like arrangement of the surfactant molecules containing primary amines as functional groups able to interact as ligands with iron cations, but also among them by H-bonding.

Assessing the chemical nature of DDA as a ligand to complete the coordination sphere of the oxidized Fe^{3+} , the nitrogenous functional group (primary amine) may be considered as a medium-force electron donor unable to fully stabilize all the positive charge on the NP's surface. In this scenario, the surface disorder reduction is not highly efficient, resulting in the slight decrease of M_s observed for the Fe_3O_4 @DDA NPs. A similar observation where the presence of an interface induced an additional surface anisotropy was reported [40]. On the other hand, the increased coercivity H_c exhibited by the coated NPs may be associated with the shape anisotropy generated by the unequal interaction of DDA with the magnetite surface. From our simulation outcomes shown below, depending on the distance, two different interactions between the surface of the NP and DDA may be identified. At short distances, the possible coordination of DDA, while at longer distances, its physical adsorption. These irregularities produce a higher anisotropy energy and hence, enhanced H_c values as the observed for the Fe_3O_4 @DDA NPs. The coating effect on the magnetic properties of Fe_3O_4 @DDA NPs render these nanostructures as potential stimuli-response materials for diverse applications, including the biomedical.

Regarding the effect of size, generally a direct relation between the anisotropy energy barriers and the coercivity relates to NPs small enough to exhibit single domains [41].

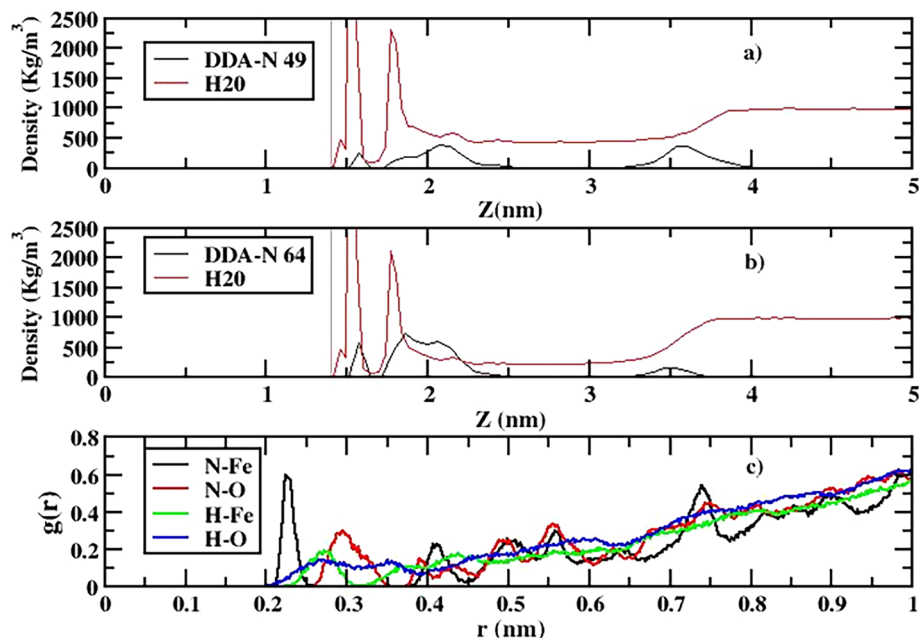
Molecular Dynamics (MD) simulations

Using as input the experimental data of atomic positions obtained by XDR and TEM analysis, an accurate theoretical model was constructed to investigate the interaction of DDA on the magnetite surface [111] facet by MD simulations. The adsorption events were analyzed using the density profiles along the perpendicular direction of the interface. As a first screening, several simulations were conducted with different numbers of DDA molecules. At low DDA concentrations (around 16 molecules) was observed a DDA divergence away from the NPs surface, while at higher concentrations of DDA occurred almost preferentially an agglomeration between them, without interaction with the NP (Fig. S3, supplementary material). Based on those results, we focused on intermediate concentrations of DDA. The density profiles of the DDA nitrogenous head-polar groups corresponding to the simulated systems with 49 and 64 DDA molecules are shown in Fig. 6a and b. From the figures, two peaks corresponding to the DDA-nitrogen are observed, indicating a nearly perpendicular location of the amine groups regarding the surface, forming a bilayer-like structure interacting with the magnetite. This result is supported by the TGA analysis indicating the presence of a DDA bilayer.

For 49 DDA molecules, the arrangement is more symmetric than the one with 64 DDA. The profiles may be related to optimal molar ratios of DDA able to arrange perpendicular to the surface of the magnetite [111] facet.

Additional information can be obtained from the two peaks in red depicted in the profiles that may be associated with two well-defined water layers close to the magnetite surface, possibly interacting by

Figure 6 Density profiles of the nitrogen site in the DDA-headgroup for **a** 49 and **b** 64 amine groups, **c** Pair distribution function ($g(r)$) of DDA-nitrogen and DDA-hydrogen with Fe and O in the magnetite [111] facet. The water profile is represented in red.



H-bonding. Furthermore, by measuring the distance between the two peaks corresponding to the density of nitrogen groups, we were able to estimate the thickness of the DDA layer close to 4 nm, which is similar to the assessed by the TEM images (Fig. 2a and 2f).

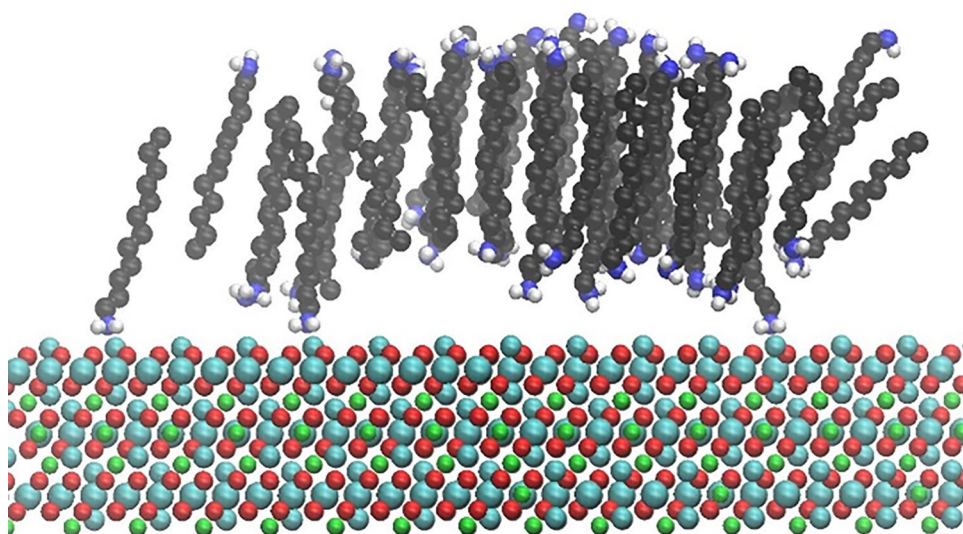
Figure 6c shows the pair correlation function plotted to calculate the distance between DDA molecules and the magnetite surface. The minimum distance between the nitrogen atoms of DDA and Fe³⁺ cations of magnetite is about 2.2 Å, which is also consistent with the organic coating dimensions observed by TEM. Summarizing, DDA molecules not only may be

interacting chemically with Fe³⁺ cations of magnetite [111] facets but also may be physically adsorbed in the form of a bilayer structure, as shown in Fig. 7.

Biological assays

The possible biomedical application is an attractive goal when have been successfully obtained coated-iron oxide magnetic NPs. To initiate this exploratory endeavor, we focused on assessing the cytotoxic impact exerted by the synthesized Fe₃O₄@DDA NPs

Figure 7 Snapshot of the interaction of DDA molecules with magnetite [111] facet. Oxygen is represented in red, Fe²⁺ in light green, Fe³⁺ in dark green, carbon in black, hydrogen in white and nitrogen in blue color.



on HepG2 cells, with the Fe_3O_4 NPs as comparative reference.

The effect of pristine and functionalized Fe_3O_4 NPs on the viability of a variety of cell lines has been widely reported. In most of these studies, the cytotoxic effect has been assessed through the MTT method [21]. The MTT assay is a versatile, low-cost, and easy-to-perform technique that indirectly measures cell viability by a semiquantitative determination of the metabolic activity of either viable or damaged cells, which might lead to a bias in cell viability [42]. Hence, in this study, we opted to employ the live/dead assay by using calcein AM and PI double staining as the primary approach for our biological significance. Calcein AM is a non-fluorescent molecule retained by active metabolic cells and converted to green-fluorescent calcein after hydrolysis by intracellular cytoplasmic esterases. Conversely, PI is a membrane-impermeable dye. Therefore, if cells lose membrane integrity, PI penetrates the cells and binds to nucleic acids, resulting in a red fluorescent signal that can be detected mainly in the nucleus. The coincidence of both signals indicates non-viable cells [43]. In that way, the calcein AM/PI assay can distinguish live and dead cells, thus becoming useful for detecting the effects of treatments that may affect cell viability or induce cell death, unlike the indirect MTT assay. In contrast to the MTT assay, which provides a snapshot of cell viability at a specific time point, calcein AM/PI staining does not require cell lysis. Therefore, it can be used to monitor cell viability over time without affecting the cells, an aspect evaluated within the framework of the present study.

Several studies have investigated the effects of Fe_3O_4 NPs on a diversity of cell lines, including HepG2 cells, although data have been somewhat contradictory. Some of them have reported that exposure to Fe_3O_4 NPs can lead to cytotoxicity and oxidative stress environment in HepG2 cells [44, 45]. Nevertheless, other studies have found slight to no effects on this cell line [46–51]. It is essential to consider that the specific effects of Fe_3O_4 NPs on HepG2 cells can vary depending on various factors such as NP size, charge, concentration, exposure, or other experimental conditions. In this study, we present the viability of cells exposed to Fe_3O_4 and Fe_3O_4 @DDA using the live/dead cell calcein AM/PI double staining (Fig. 8).

Figure 8 shows that following 72 h of incubation with non-coated Fe_3O_4 NPs up to a concentration of 300 $\mu\text{g}/\text{mL}$, the percentage of live cells remained as

high as 80% of viability (See Table S1 for % cell viability values).

The highest concentration used in this study, 300 $\mu\text{g}/\text{mL}$, was selected based on the work conducted by Huang et al., which investigated the impact of asialoglycoprotein-functionalized iron oxide NPs on HepG2 cells viability in a broad concentration range (0.03–3000 $\mu\text{g}/\text{mL}$) which included that of 300 $\mu\text{g}/\text{mL}$, along with prolonged incubation times (up to five days of culture) without significant effects on cell viability [51]. Our results align with the aforementioned study and are consistent with other research articles that have reported a favorable cytocompatibility profile on HepG2 cells with iron oxide np, despite differences in np characteristics and experimental methods [46–50]. As far as we know, this is the first report of assessing the viability of cells in the presence of pristine Fe_3O_4 NPs using live/dead assay, showing that Fe_3O_4 does not affect the viability of HepG2 cells significantly.

Figure 9 depicts the cellular response to Fe_3O_4 @DDA NPs. At a 10 $\mu\text{g}/\text{mL}$ concentration, the coated NPs did not exhibit any evident impact on HepG2 cells even after 72 h of incubation. In fact, the percentage of cell viability was comparable to that of Fe_3O_4 NPs. When the concentration of Fe_3O_4 @DDA increased to 50 $\mu\text{g}/\text{mL}$, the population of viable cells was similar to the control at 24 h. However, after 48 h, the population of live cells considerably diminished to 63% of viability; at 72 h of incubation time, only 30% of cells were viable. This time-dependent effect can be seen qualitatively in the micrographs, which show a progressive increase in the number of cells exhibiting PI staining as the incubation time proceeds (see Table S2 for % cell viability values).

Remarkably, a dramatic effect was observed when the cells were exposed to 300 $\mu\text{g}/\text{mL}$ Fe_3O_4 @DDA. After 24 h, barely any of the initial cultured cells remained viable (< 10%), and at 48 h of culture, no viable cells were detected. The micrographs did not show any PI staining, as the cells were likely completely detached from coverslips. These data evidenced the effect of DDA on HepG2 cells viability at concentrations of > 50 $\mu\text{g}/\text{mL}$ Fe_3O_4 @DDA.

DDA is a long-chain primary amine with a 12-carbon alkyl chain. DDA is commonly used as a surfactant, emulsifier, or dispersing agent in various applications [52]. DDA and some of its derivatives have exhibited antibacterial activity against both Gram-positive and Gram-negative bacteria as well as fungi [52–54]. DDA has also been employed as

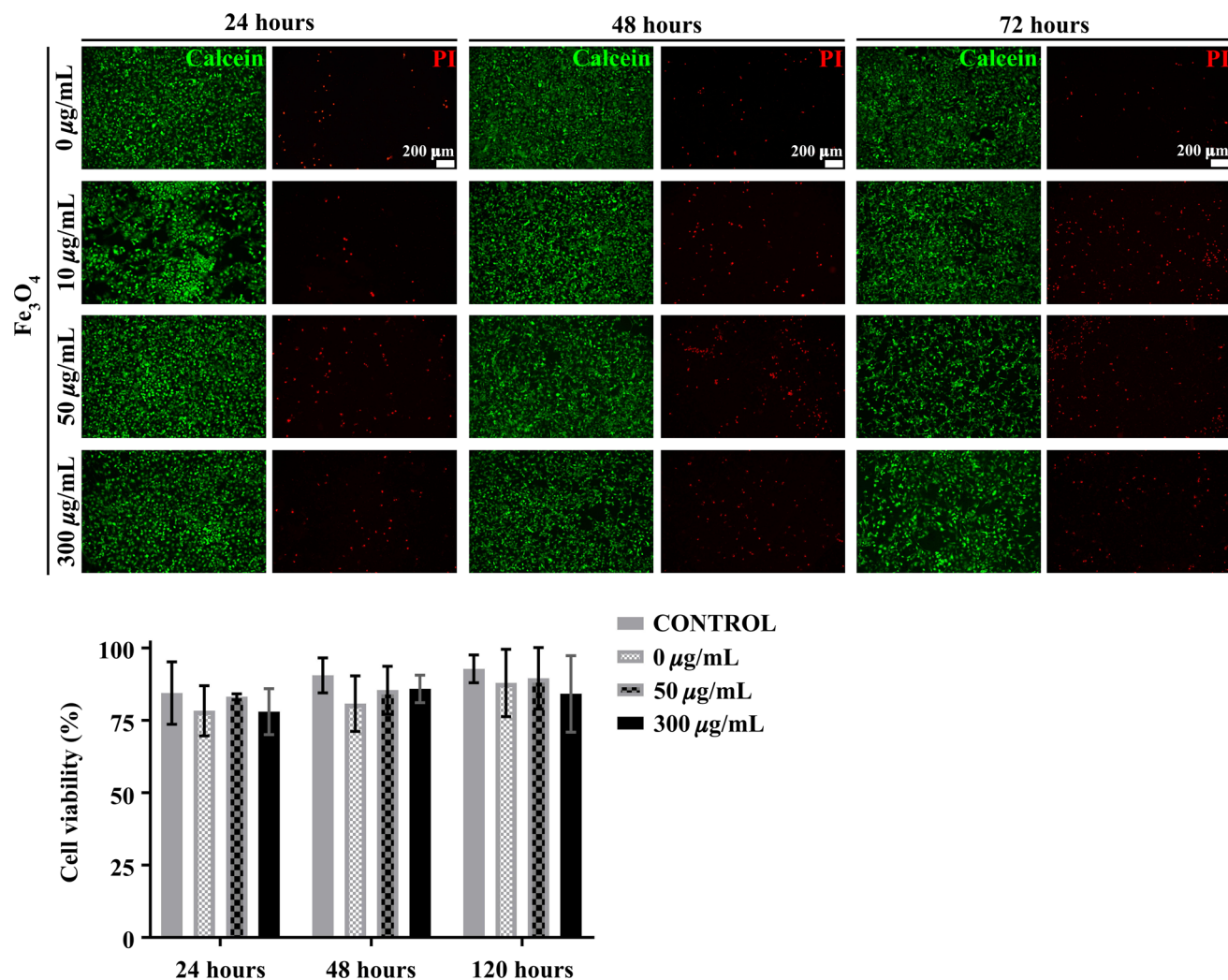


Figure 8 The viability of HepG2 cells in the presence of Fe_3O_4 at 10, 50 and 300 $\mu\text{g}/\text{mL}$ after 24, 48 and 72 h incubation time. The cells viability was determined through live/dead calcein

AM/PI double staining assay. Calcein AM (in green) shows alive cells, while propidium iodide (PI) indicates dead cells. The results were considered statistically significant when $p < 0.05$.

a building block for constructing nano-assemblies aimed at inhibiting cancer cells [55–57]. In a study conducted by Wang et al., DDA is conjugated with phosphotyrosine, resulting in a synthetic lipid capable of self-assembling into micelles. Upon enzymatic dephosphorylation, the DDA-based lipid is released, incorporating itself into the cell membrane and subsequently increasing the cell membrane tension, thus activating multiple cell death pathways. The aforementioned micelles were evaluated in HepG2 cells, resulting in an IC_{50} value of 45.2 μM [58].

In the present work, DDA is attached to the iron oxide nuclei, and our findings unambiguously demonstrate that DDA coating induces cell death in HepG2 cells. Consequently, Fe_3O_4 @DDA NPs may potentially

exhibit synergistic effects by further combining the cytotoxicity of DDA plus the magnetic hyperthermia generated after exposing the NPs to an alternating magnetic field. In this direction, we evaluated whether Fe_3O_4 @DDA NPs might promote apoptosis in the concentration of 10 or 50 $\mu\text{g}/\text{mL}$ where HepG2 cells still adhere to the coverslip. To that aim we performed the Terminal deoxynucleotidyl transferase (TdT) dUTP Nick-End Labeling (TUNEL) assay in order to seek for double-strand breaks in genomic DNA, a standard reference of apoptotic cells. Unfortunately, we did not observe significant induction of apoptosis by neither Fe_3O_4 nor Fe_3O_4 @DDA NPs at 50 $\mu\text{g}/\text{mL}$ for 72 h of culture (Fig. 10a). We used sulforaphane (SNF) as a positive control because it is known to induce cell

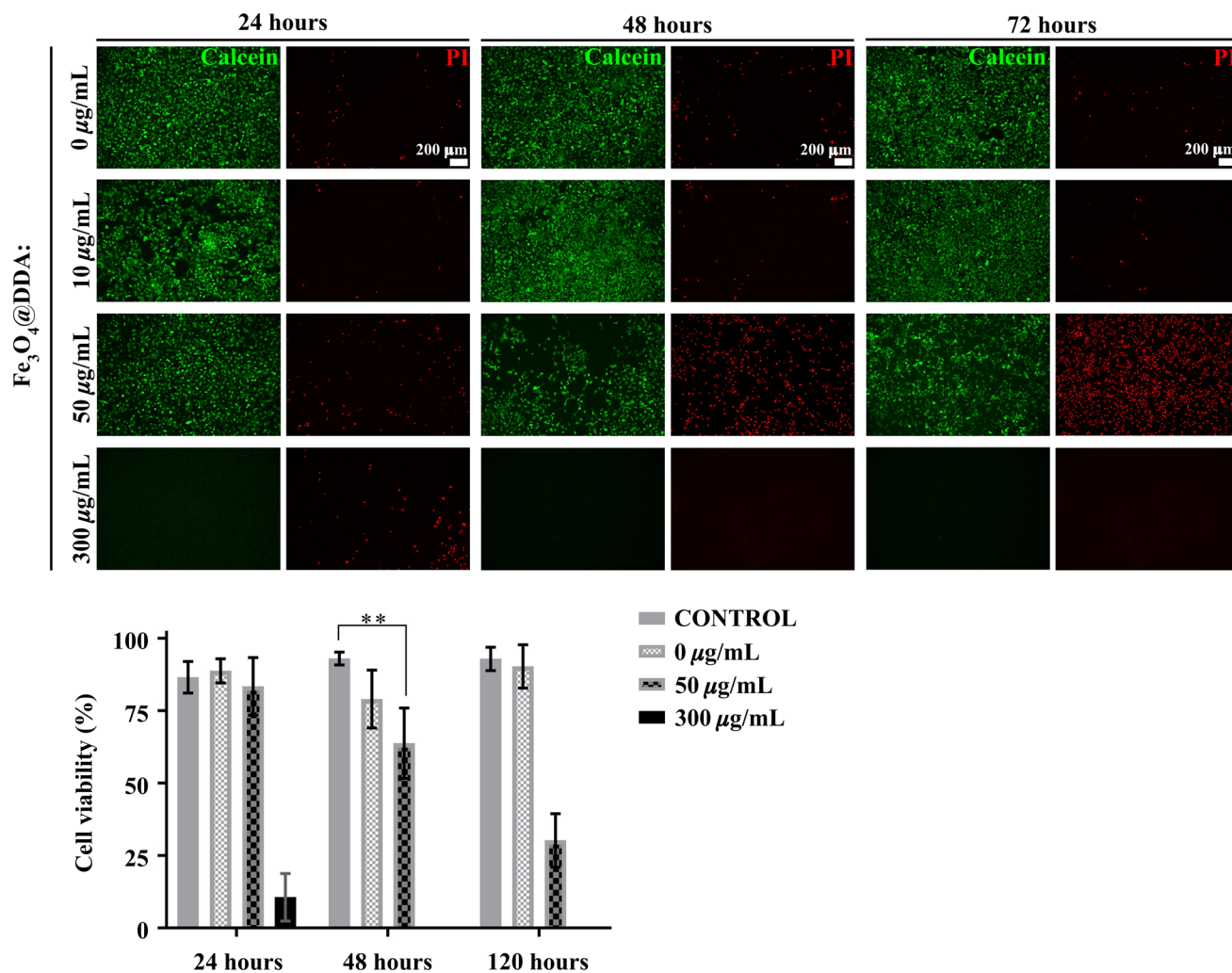


Figure 9 The viability of HepG2 cells in the presence of $\text{Fe}_3\text{O}_4@DDA$ at 10, 50 and 300 $\mu\text{g/mL}$ after 24, 48 and 72 h incubation time. The cells viability was determined through live/dead calcein AM/PI double staining assay. Calcein AM (in

green) shows alive cells, while propidium iodide (PI) indicates dead cells. Results were considered statistically significant when $p < 0.05$.

death by reducing reactive oxygen species (ROS) that are necessary to cell viability in HepG2 cells [59]. It is possible that apoptosis machinery is not involved in the mechanism of cell damage induced by $\text{Fe}_3\text{O}_4@DDA$ NPs and other targets could be participating such as plasmatic membrane integrity.

The surfactant-like properties of DDA might disturb the integrity of cell lipid bilayer structure, leading to altered permeability and a strong cell death effect. This mechanism is consistent with the observations depicted in Fig. 9, where cells exhibited PI staining following exposure to $\text{Fe}_3\text{O}_4@DDA$ at a concentration of 50 $\mu\text{g/mL}$. To further substantiate this statement, we conducted a trypan blue dye exclusion

assay in which, similar to PI, viable cells with non-permeable membranes exclude the polar dye and are shown unstained [60, 61]. On the other hand, cells with compromised membranes allow trypan blue to enter and accumulate within the cells, resulting in visible blue staining accumulated at the nucleus. For the trypan blue assay, we worked at the concentration of 300 $\mu\text{g/mL}$ of both Fe_3O_4 and $\text{Fe}_3\text{O}_4@DDA$ at brief periods of time; we also evaluated DDA at 72 $\mu\text{g/mL}$, a concentration equivalent to the highest percentage of DDA coating obtained after our synthetic procedure [16]. In parallel, we performed calcein AM/PI double staining assay (at 300 $\mu\text{g/mL}$ and 1,3 and 5 h incubation time) to couple membrane

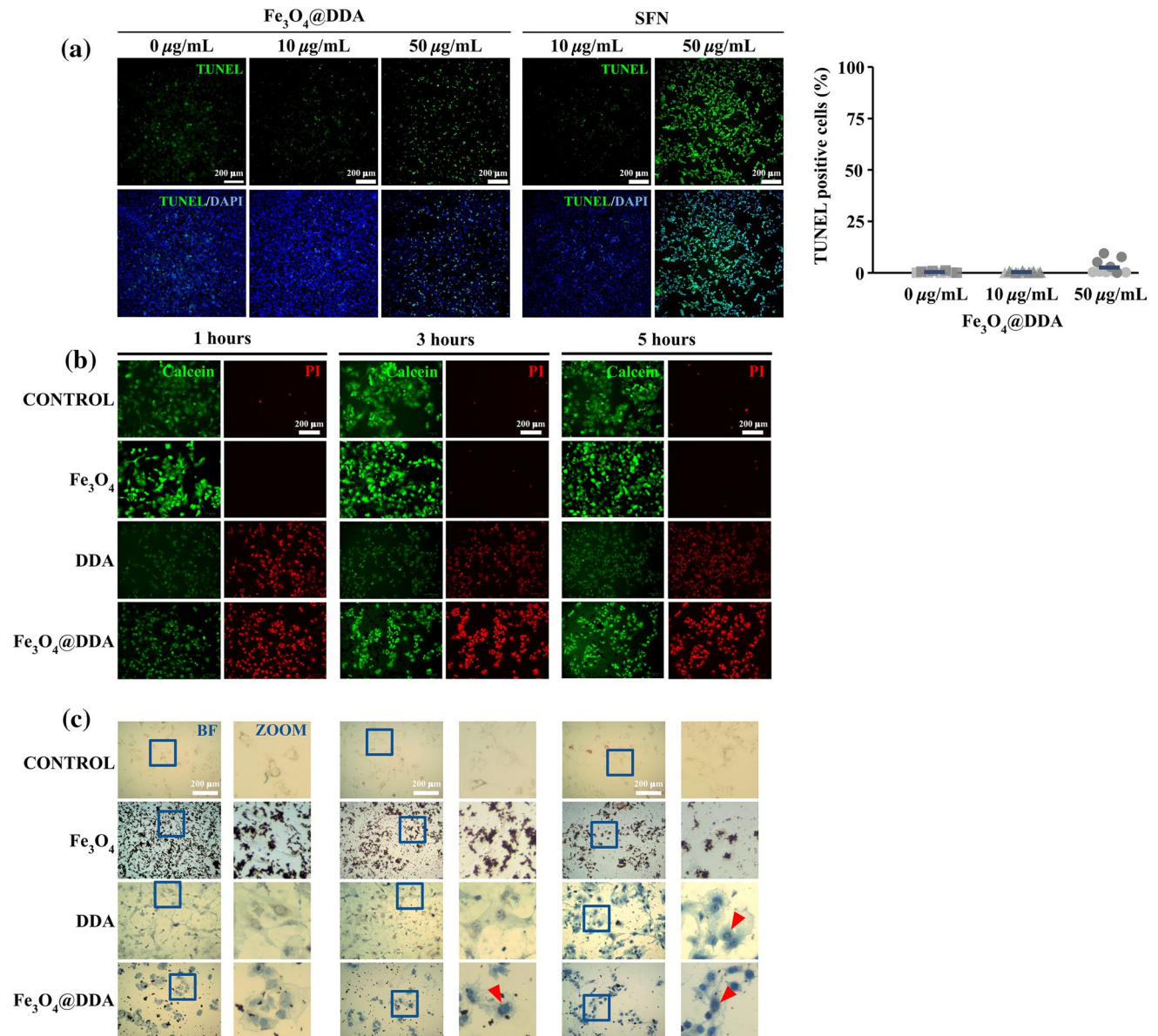


Figure 10 **a** Terminal deoxynucleotidyl transferase (TdT) dUTP Nick-End Labeling (TUNEL) assay was performed in HepG2 cells incubated with 10 and 50 $\mu\text{g/mL}$ of Fe_3O_4 and $\text{Fe}_3\text{O}_4@DDA$ for 72 h of culture. Sulforaphane (SNF) was used as positive control for TUNEL (green), whereas DAPI was used as a nuclear reference (blue). Positive cells to double-strand DNA breaks (TUNEL/DAPI) were quantified and plotted as percentages. **b** Assessment of HepG2 cells membrane integrity by trypan blue

dye exclusion staining in a time course (1–5 h) after the exposure of Fe_3O_4 and $\text{Fe}_3\text{O}_4@DDA$ at 300 $\mu\text{g/mL}$; and DDA at 72 $\mu\text{g/mL}$. Cells with compromised membrane integrity are stained in blue. **c** Cell membrane damage confirmed by live/dead calcein AM/PI double staining assay. Calcein AM (in green) shows alive cells with intact membranes; propidium iodide (PI) distinguishes dead cells with leaky membranes.

damage with cell viability caused by DDA and $\text{Fe}_3\text{O}_4@DDA$.

Figure 10b evidences how $\text{Fe}_3\text{O}_4@DDA$ compromised the cell membrane integrity as early as 1 h of incubation; HepG2 cells were stained in blue as

indicative of permeable plasmatic cell membranes. This effect is also shown in HepG2 cells incubated with DDA alone but at 5 h afterward, when nuclei are significantly stained, suggesting that the effect of DDA potentiates when is attached to the Fe_3O_4 nuclei. No

significant staining was observable in the vehicle or Fe₃O₄ treatments. In Fig. 10c, calcein AM/PI double staining allowed us to observe that DDA caused cell damage since the first 1 h of incubation and remained up to 5 h of incubation. Interestingly, a similar effect was observed for Fe₃O₄@DDA. To note, at 5 h of incubation is possible to observe residual cells stained with PI, unlike 24 h of culture when cells seemed to detach from the coverslip (see Fig. 9), indicating severe cell damage. Through these experiments, we also confirmed that Fe₃O₄ did not affect the membrane integrity of HepG2 cells even at the concentration of 300 µg/mL.

Cell membranes have emerged as novel targets for antineoplastic agents over the past two decades. This promising approach in the field of anticancer drug development involves compounds primarily interfering with cell membranes integrity. By modulating membrane permeability and fluidity, as well as altering membrane lipid composition, phospholipid metabolism, and proliferation signal transduction, these potential anticancer compounds hold great potential for therapeutic efficacy [62, 63].

Conclusions

The tetrahedral Fe³⁺ cations exposed on the thermodynamically most stable surface of magnetite ([111] facets), impose the interaction fashion of magnetite NPs with DDA coating, which behaves as a ligand but also as a surfactant, forming bilayers by self-interacting through H-bonding and dispersion interactions. DDA shapes the inner and outer surface of the bilayer, and this ordering may be associated with the NPs anisotropy.

A coating bilayer of 4–5 nm thickness observed by TEM images was organized in a perpendicular disposition of DDA molecules on the surface of Fe₃O₄ NPs. The ordering of DDA molecules was corroborated with MD simulations, confirming the DDA's dissimilar interactions at the magnetite NP interface.

This organic layer preserves the magnetic functionality of the NPs (i.e., high magnetization values—well over 40 emu/g— together with small coercivity fields —below 20 Oe—).

Fe₃O₄ nanoparticles showed good compatibility with HepG2 cells, aligning with previous studies and confirming their suitability for biomedical applications. However, introducing DDA

moieties significantly increased their cytotoxicity against HepG2 cells. This hints at DDA's pivotal role in causing cell death, possibly through its amine groups interacting with the cell membrane's lipid bilayer, disrupting its integrity. The outcomes of both, TUNEL and Trypan blue assay point out the compromised membrane integrity as the primary mechanism of HepG2 cell death. Further investigations are needed to reveal underlying molecular mechanisms at biological interfaces to exploit the potential of Fe₃O₄@DDA nanoparticles as an anticancer strategy in the nanomedicine field.

Acknowledgements

Authors acknowledge Engineer Karla Eriseth Reyes Morales for the thermal analyses and MSc. Adriana Tejada Cruz the X-ray diffractograms acquisition, as well as Dr. Jesus Arenas from IF-UNAM for magnetic measurements assistance. Y. R-A thanks to the financial support from Instituto de Investigaciones en Materiales, Universidad Nacional Autónoma de México (UNAM) (1306-IIM Project); M. M-A thanks to Consejo Nacional de Ciencia y Tecnología (CONACYT) and UNAM for the Msc. scholarship CVU-1034837; G. V-V thanks to Programa de Apoyo a Proyectos de Investigación e Innovación Tecnológica (PAPIIT-IN21972) and National Laboratory LaNSBioDyT-CONAHCyT for technical support. HD acknowledges DGTIC-UNAM LANCAD-UNAM-DGTIC-238 for supercomputer facilities. PG acknowledges the financial support from Instituto de Investigaciones en Materiales, Universidad Nacional Autónoma de México (UNAM) (1316-IIM Project).

Author contributions

YRA Conception and planning of the work, manuscript writing, analysis and interpretation of the data. PG Conception and planning of the work, manuscript writing, analysis and interpretation of the data, drafting and critical revision. JR Analysis and interpretation of the data, art work, drafting. RMC Microscopy measurements and interpretation of the data. ARH, BDB and GVV Biological experiments and interpretation of the data. HD and IB Theoretical and magnetic results, respectively, interpretation of the data and

critical revision. MMA and SOG interpretation of the data and assistance in the reference format.

Data availability

Not applicable.

Declarations

Conflict of interest Authors declare that no conflicts of interest exist.

Ethical approval Not applicable.

Supplementary Information The online version contains supplementary material available at <https://doi.org/10.1007/s10853-023-09235-3>.

Open Access This article is licensed under a Creative Commons Attribution 4.0 International License, which permits use, sharing, adaptation, distribution and reproduction in any medium or format, as long as you give appropriate credit to the original author(s) and the source, provide a link to the Creative Commons licence, and indicate if changes were made. The images or other third party material in this article are included in the article's Creative Commons licence, unless indicated otherwise in a credit line to the material. If material is not included in the article's Creative Commons licence and your intended use is not permitted by statutory regulation or exceeds the permitted use, you will need to obtain permission directly from the copyright holder. To view a copy of this licence, visit <http://creativecommons.org/licenses/by/4.0/>.

References

- Niculescu A-G, Chircov C, Grumezescu AM (2022) Magnetite nanoparticles: synthesis methods—a comparative review. *Methods* 199:16–27. <https://doi.org/10.1016/j.ymeth.2021.04.018>
- Jjagwe J, Olupot PW, Carrara S (2023) Iron oxide nanoparticles/nanocomposites derived from steel and iron wastes for water treatment: a review. *J Environ Manage* 343:118236. <https://doi.org/10.1016/j.jenvman.2023.118236>
- Ng N, Wan Ibrahim WA, Sutirman ZA et al (2023) Magnetic nanomaterials for preconcentration and removal of emerging contaminants in the water environment. *Nanotechnol Environ Eng* 8:297–315. <https://doi.org/10.1007/s41204-022-00296-4>
- Kumar NS, Suvarna RP, Babu Naidu KC, Reddy BVS (2022) Magnetic nanoparticles for high energy storage applications. *Fundamentals and Industrial Applications of Magnetic Nanoparticles*. Elsevier, Amsterdam, pp 601–618
- Praharaj S, Rout D (2022) Magnetic nanoparticles in catalysis industry. *Fundamentals and Industrial Applications of Magnetic Nanoparticles*. Elsevier, Amsterdam, pp 477–495
- Balaban Hanoglu S, Harmanci D, Ucar N et al (2023) Recent approaches in magnetic nanoparticle-based biosensors of miRNA detection. *Magnetochemistry* 9:23. <https://doi.org/10.3390/magnetochemistry9010023>
- Adampourezare M, Hasanzadeh M, Hoseinpourefeizi MA, Seidi F (2023) Iron/iron oxide-based magneto-electrochemical sensors/biosensors for ensuring food safety: recent progress and challenges in environmental protection. *RSC Adv* 13:12760–12780
- Setia A, Mehata AK, Vikas, et al (2023) Theranostic magnetic nanoparticles: synthesis, properties, toxicity, and emerging trends for biomedical applications. *J Drug Deliv Sci Technol* 81:104295. <https://doi.org/10.1016/j.jddst.2023.104295>
- Alphandéry E (2020) Iron oxide nanoparticles for therapeutic applications. *Drug Discov Today* 25:141–149. <https://doi.org/10.1016/j.drudis.2019.09.020>
- Jing X, Zhang Y, Li M et al (2023) Surface engineering of colloidal nanoparticles. *Mater Horiz* 10:1185–1209. <https://doi.org/10.1039/D2MH01512A>
- Hazra C, Kundu D, Chatterjee A (2018) Stimuli-responsive nanocomposites for drug delivery. *Appl Nanocompos Mater Drug Deliv*. <https://doi.org/10.1016/B978-0-12-813741-3.00036-4>
- Aslam H, Shukrullah S, Naz MY et al (2022) Current and future perspectives of multifunctional magnetic nanoparticles based controlled drug delivery systems. *J Drug Deliv Sci Technol* 67:102946. <https://doi.org/10.1016/J.JDDST.2021.102946>
- Gambhir RP, Rohiwal SS, Tiwari AP (2022) Multifunctional surface functionalized magnetic iron oxide nanoparticles for biomedical applications: a review. *Appl Surf Sci Adv*. <https://doi.org/10.1016/j.apsadv.2022.100303>
- Abdolrahimi M, Vasilakaki M, Slimani S et al (2021) Magnetism of nanoparticles: effect of the organic coating.

- Nanomaterials 11:1787. <https://doi.org/10.3390/nano11071787>
- [15] Lima E, Brandl AL, Arelaro AD, Goya GF (2006) Spin disorder and magnetic anisotropy in Fe₃O₄ nanoparticles. *J Appl Phys* DOI. <https://doi.org/10.1063/1.2191471>
- [16] Cruz-Vargas J, Belmont-Bernal F, Vera-De La Garza CG et al (2018) Accelerated one-pot synthesis of coated magnetic nanoparticles from iron(ii) as a single precursor. *New J Chem* 42:13107–13113. <https://doi.org/10.1039/c8nj02270d>
- [17] Vestal CR, Zhang ZJ (2003) Effects of surface coordination chemistry on the magnetic properties of MnFe₂O₄ spinel ferrite nanoparticles. *J Am Chem Soc*. <https://doi.org/10.1021/ja035474n>
- [18] Yuan Y, Rende D, Altan CL et al (2012) Effect of surface modification on magnetization of iron oxide nanoparticle colloids. *Langmuir*. <https://doi.org/10.1021/la3022479>
- [19] Nikolova MP, Joshi PB, Chavali MS (2023) Updates on biogenic metallic and metal oxide nanoparticles: therapy. *Drug Deliv Cytotox Pharm* 15:1650. <https://doi.org/10.3390/pharmaceutics15061650>
- [20] Frtús A, Smolková B, Uzhytchak M et al (2020) Analyzing the mechanisms of iron oxide nanoparticles interactions with cells: a road from failure to success in clinical applications. *J Control Release* 328:59–77. <https://doi.org/10.1016/j.jconrel.2020.08.036>
- [21] Dragar Č, Kralj S, Kocbek P (2021) Bioevaluation methods for iron-oxide-based magnetic nanoparticles. *Int J Pharm* 597:120348. <https://doi.org/10.1016/j.ijpharm.2021.120348>
- [22] Lunova M, Smolková B, Lynnyk A et al (2019) Targeting the mTOR signaling pathway utilizing nanoparticles: a critical overview. *Cancers (Basel)* 11:82. <https://doi.org/10.3390/cancers11010082>
- [23] Zavisova V, Koneracka M, Kovac J et al (2015) The cytotoxicity of iron oxide nanoparticles with different modifications evaluated in vitro. *J Magn Magn Mater* 380:85–89. <https://doi.org/10.1016/j.jmmm.2014.10.041>
- [24] Tran N, Webster TJ (2010) Magnetic nanoparticles: biomedical applications and challenges. *J Mater Chem* 20:8760. <https://doi.org/10.1039/c0jm00994f>
- [25] Konuk M, Sellschopp K, Vonbun-Feldbauer GB, Meißner RH (2021) Modeling charge redistribution at magnetite interfaces in empirical force fields. *J Phys Chem C* 125:4794–4805. <https://doi.org/10.1021/acs.jpcc.0c10338>
- [26] Tombácz E, Hajdú A, Illés E et al (2009) Water in contact with magnetite nanoparticles, as seen from experiments and computer simulations. *Langmuir* 25:13007–13014. <https://doi.org/10.1021/la901875f>
- [27] Brown ZJ, Tsilimigras DI, Ruff SM et al (2023) Management of hepatocellular carcinoma: a review. *JAMA Surg* 158:410–420. <https://doi.org/10.1001/jamasurg.2022.7989>
- [28] Espinosa-Jiménez H, Salazar-Arriaga AB, Dominguez H (2023) Development of a new force field for the family of primary aliphatic amines using the three steps systematic parameterization procedure. *Condens Matter Phys*. <https://doi.org/10.5488/CMP.26.23603>
- [29] Berendsen HJC, Grigera JR, Straatsma TP (1987) The missing term in effective pair potentials. *J Phys Chem* 91:6269–6271. <https://doi.org/10.1021/j100308a038>
- [30] Hess B, Kutzner C, Van Der Spoel D, Lindahl E (2008) GRGMACS 4: Algorithms for highly efficient, load-balanced, and scalable molecular simulation. *J Chem Theory Comput* 4:435–447. <https://doi.org/10.1021/ct700301q>
- [31] Eustaquio T, Leary JF (2016) Nanobarcode superparamagnetic iron oxide nanoparticles for nanomedicine: Quantitative studies of cell-nanoparticle interactions by scanning image cytometry. *Cytometry A* 89:207–216. <https://doi.org/10.1002/cyto.a.22699>
- [32] Wu W, Wu Z, Yu T et al (2015) Recent progress on magnetic iron oxide nanoparticles: Synthesis, surface functional strategies and biomedical applications. *Sci Technol Adv Mater* 16:023501
- [33] Hu L, Ren X, Yang M, Guo W (2021) Facet-controlled activation of persulfate by magnetite nanoparticles for the degradation of tetracycline. *Sep Purif Technol*. <https://doi.org/10.1016/j.seppur.2020.118014>
- [34] Holder CF, Schaak RE (2019) Tutorial on powder x-ray diffraction for characterizing nanoscale materials. *ACS Nano* 13:7359–7365. <https://doi.org/10.1021/acsnano.9b05157>
- [35] Santos-Carballal D, Roldan A, Grau-Crespo R, de Leeuw NH (2014) A DFT study of the structures, stabilities and redox behaviour of the major surfaces of magnetite Fe₃O₄. *Phys Chem Chem Phys* 16:21082–21097. <https://doi.org/10.1039/c4cp00529e>
- [36] Yang T, Wen XD, Ren J et al (2010) Surface structures of Fe₃O₄ (111), (110), and (001)—a density functional theory study. *Ranliao Huaxue Xuebao/J Fuel Chem Technol* 38:121–128. [https://doi.org/10.1016/s1872-5813\(10\)60024-2](https://doi.org/10.1016/s1872-5813(10)60024-2)
- [37] Creutzburg M, Sellschopp K, Gleißner R et al (2022) Surface structure of magnetite (111) under oxidizing and reducing conditions. *J Phys Cond Matter*. <https://doi.org/10.1088/1361-648X/ac4d5a>
- [38] Horák D, Pustovyy VI, Babinskyi AV et al (2017) Enhanced antitumor activity of surface-modified iron oxide nanoparticles and an α -tocopherol derivative in a rat model of mammary gland carcinosarcoma. *Int J Nanomed* 12:4257–4268. <https://doi.org/10.2147/IJN.S137574>

- [39] Arora V, Sood A, Shah J et al (2017) Synthesis and characterization of pectin-6-aminohexanoic acid-magnetite nanoparticles for drug delivery. *Mater Sci Eng C* 80:243–251. <https://doi.org/10.1016/j.msec.2017.05.097>
- [40] Umut E, Pineider F, Arosio P et al (2012) Magnetic, optical and relaxometric properties of organically coated gold-magnetite (Au-Fe₃O₄) hybrid nanoparticles for potential use in biomedical applications. *J Magn Magn Mater* 324:2373–2379. <https://doi.org/10.1016/j.jmmm.2012.03.005>
- [41] Singh S, Munjal S, Khare N (2015) Strain/defect induced enhanced coercivity in single domain CoFe₂O₄ nanoparticles. *J Magn Magn Mater* 386:69–73. <https://doi.org/10.1016/j.jmmm.2015.03.057>
- [42] van Meerloo J, Kaspers GJL, Cloos J (2011) Cell Sensitivity Assays: The MTT Assay. In: Cree IA (ed) *Cancer Cell Culture: Methods and Protocols*. Humana Press, Totowa, NJ, pp 237–245
- [43] Chan LL, Wilkinson AR, Paradis BD, Lai N (2012) Rapid image-based cytometry for comparison of fluorescent viability staining methods. *J Fluoresc* 22:1301–1311. <https://doi.org/10.1007/s10895-012-1072-y>
- [44] Sadeghi L, Tanwir F, Yousefi Babadi V (2015) In vitro toxicity of iron oxide nanoparticle: oxidative damages on Hep G2 cells. *Exp Toxicol Pathol* 67:197–203. <https://doi.org/10.1016/j.etp.2014.11.010>
- [45] Patil RM, Thorat ND, Shete PB et al (2018) Comprehensive cytotoxicity studies of superparamagnetic iron oxide nanoparticles. *Biochem Biophys Rep* 13:63–72
- [46] Qu JB, Shao HH, Jing GL, Huang F (2013) PEG-chitosan-coated iron oxide nanoparticles with high saturated magnetization as carriers of 10-hydroxycamptothecin: preparation, characterization and cytotoxicity studies. *Colloids Surf B Biointerfaces* 102:37–44. <https://doi.org/10.1016/j.colsurfb.2012.08.004>
- [47] Sudame A, Kandasamy G, Singh D et al (2020) Symbiotic thermo-chemotherapy for enhanced HepG2 cancer treatment via magneto-drugs encapsulated polymeric nanocarriers. *Colloids Surf A Physicochem Eng Asp*. <https://doi.org/10.1016/j.colsurfa.2020.125355>
- [48] Hedayatnasab Z, Dabbagh A, Abnisa F, Wan Daud WMA (2020) Synthesis and in-vitro characterization of superparamagnetic iron oxide nanoparticles using a sole precursor for hyperthermia therapy. *Mater Res Bull*. <https://doi.org/10.1016/j.materresbull.2020.110975>
- [49] Kandasamy G, Soni S, Sushmita K et al (2019) One-step synthesis of hydrophilic functionalized and cytocompatible superparamagnetic iron oxide nanoparticles (SPIONs) based aqueous ferrofluids for biomedical applications. *J Mol Liq* 274:653–663. <https://doi.org/10.1016/j.molliq.2018.10.161>
- [50] Peng X, Wang B, Yang Y et al (2019) Liver tumor spheroid reconstitution for testing mitochondrial targeted magnetic hyperthermia treatment. *ACS Biomater Sci Eng* 5:1635–1644. <https://doi.org/10.1021/acsbiomaterials.8b01630>
- [51] Huang G, Diakur J, Xu Z, Wiebe LI (2008) Asialoglycoprotein receptor-targeted superparamagnetic iron oxide nanoparticles. *Int J Pharm* 360:197–203. <https://doi.org/10.1016/j.ijpharm.2008.04.029>
- [52] Li Z, Wang X, Miao J et al (2022) Antibacterial activity of dodecylamine dialdehyde starch schiff base derivatives. *Starch/Staerke*. <https://doi.org/10.1002/star.202100178>
- [53] Koziróg A, Brycki B, Pielech-Przybylska K (2018) Impact of cationic and neutral gemini surfactants on conidia and hyphal forms of *Aspergillus brasiliensis*. *Int J Mol Sci*. <https://doi.org/10.3390/ijms19030873>
- [54] Mokashi S, Kanaan J, Craft DL et al (2020) Killing of bacterial spores by dodecylamine and its effects on spore inner membrane properties. *J Appl Microbiol* 129:1511–1522. <https://doi.org/10.1111/jam.14732>
- [55] Sun J, Li M, Lin K et al (2023) Delivery of quercetin for breast cancer and targeting potentiation via hyaluronic nano micelle. *Int J Biol Macromol*. <https://doi.org/10.1016/j.ijbiomac.2023.124736>
- [56] Yu Y, Yang X, Liu M et al (2019) Anticancer drug delivery to cancer cells using alkyl amine-functionalized nanodiamond supraparticles. *Nanoscale Adv* 1:3406–3412. <https://doi.org/10.1039/c9na00453j>
- [57] Zhang Y, Wang H, Jiang H, Wang X (2012) Water induced protonation of amine-terminated micelles for direct syntheses of ZnO quantum dots and their cytotoxicity towards cancer. *Nanoscale* 4:3530–3535. <https://doi.org/10.1039/c2nr30127j>
- [58] Wang J, Tan W, Li G et al (2020) Enzymatic insertion of lipids increases membrane tension for inhibiting drug resistant cancer cells. *Chem Eur J* 26:15116–15120. <https://doi.org/10.1002/chem.202002974>
- [59] Wu J, Han J, Hou B et al (2016) Sulforaphane inhibits TGF- β -induced epithelial-mesenchymal transition of hepatocellular carcinoma cells via the reactive oxygen species-dependent pathway. *Oncol Rep*. <https://doi.org/10.3892/or.2016.4638>
- [60] Fischel's SV, Medzihradsky F (1985) Assessment of membrane permeability in primary cultures of neurons and glia in response to osmotic perturbation. *J Neurosci Res* 13:369–380. <https://doi.org/10.1002/jnr.490130304>
- [61] Kamiloglu S, Sari G, Ozdal T, Capanoglu E (2020) Guidelines for cell viability assays. *Food Front* 1:332–349. <https://doi.org/10.1002/fft2.44>

- [62] Tan LTH, Chan KG, Pusparajah P et al (2017) Targeting membrane lipid a potential cancer cure? *Front Pharmacol* 8:1–6. <https://doi.org/10.3389/fphar.2017.00012>
- [63] Jendrossek V, Handrick R (2003) Membrane targeted anti-cancer drugs: potent inducers of apoptosis and putative radiosensitisers

Publisher's Note Springer Nature remains neutral with regard to jurisdictional claims in published maps and institutional affiliations.